Anion Exchange of Ruddlesden–Popper Lead Halide Perovskites Produces Stable Lateral Heterostructures

Chris R. Roy†, Dongxu Pan†, Yining Wang‡, Matthew P. Hautzinger†, Yuzhou Zhao†, John C. Wright†, Zihua Zhu‡, and Song Jin†*

†Department of Chemistry, University of Wisconsin – Madison, 1101 University Avenue, Madison, Wisconsin 53706, United States

‡Environmental Molecular Sciences Laboratory, Pacific Northwest National Laboratory, 902 Battelle Boulevard, Richland, Washington 99352, United States

ABSTRACT: Heterostructures of three-dimensional (3D) halide perovskites are unstable because of facile anion interdiffusion at halide interfaces. Two-dimensional (2D) Ruddlesden–Popper halide perovskites (RPPs) show suppressed and anisotropic ion diffusion that could enable stable RPP heterostructures, yet the direct and general growth of lateral RPP heterostructures remains challenging. Here we show that halide miscibility in RPPs decreases with perovskite layer thickness (n), enabling the formation of sharp halide lateral heterostructures from $n = 1$ and 2 RP lead iodide microplates via anion exchange with hydrogen bromide vapor. In contrast, RPPs with $n \geq 3$ form more diffuse lateral heterojunctions, more similar to those in 3D perovskites. The anion exchange behaviors are further modulated by the spacer and A-site cations in the RPP structures. These new insights, and kinetic studies of the exchange reactions, enable the preparation of lateral heterostructures from various $n = 2$ RPPs that are more stable against anion interdiffusion and degradation for potential device applications.

INTRODUCTION

Lead halide perovskites (LHPs) have found many promising applications in solution-processable photovoltaics, light-emitting diodes (LEDs), and other optoelectronic devices[1–3] owing to their high optical densities, long charge carrier diffusion lengths, and superb defect-tolerant performance.[4,5] The most studied three-dimensional (3D) LHPs have the formula of $APbX_3$, where A is a monovalent cation and X is a halide. They readily form solid solutions of halide ions continuously spanning from the narrow band gap (~ 1.6 eV) iodide LHPs to wide band gap chloride LHPs (~ 2.9 eV).[2,6] Building on such tunable semiconductor materials, one would have envisioned the fabrication of semiconductor heterostructures that can allow the manipulation of charge carriers and serve as the foundations for high performance optoelectronic devices, analogous to heterostructures based on III-V semiconductors.[7] However, halide-based $APbX_3/APbBX'_3$ heterojunctions have been shown to interdiffuse to form alloyed $APb(X/X')_3$ spontaneously over time at room temperature, which is accelerated under extrinsic perturbations such as higher temperatures or illumination.[8–10] Moreover, mixed halide 3D LHPs could phase separate into thermodynamically favorable phases with different halide (or A cation) compositions under excitation.[11–14] Such facile anion diffusion and instability have prevented the studies and applications of halide perovskite heterostructures.

Ruddlesden–Popper perovskites (RPPs)[15] could be more promising building blocks for making heterostructures than 3D perovskites. RPPs are a family of quasi-2D layered semiconductors with the general formula $(LA)_2(A)_{n-1}Pb_nX_{3n+1}$, consisting of n layers of inorganic corner-sharing Pb-X octahedra separated by bilayers of large organic spacer cations (LA) like n-butylammonium (BA). RPPs have better environmental resilience than 3D perovskites,[16] yet also exhibit more tunable optoelectronic properties through controllable quantum confinement of the Pb-X sheets (n value),[17,18] the structural and electronic characteristics of the spacer cations,[19,20] and to a lesser degree the A-site cations.[21,22] RPPs' utility in photovoltaics,[16,23] LEDs,[24,25] and photodetectors has been demonstrated with performance competitive with—and at times superior to—3D LHPs.[3,26] The layered crystal structures of RPPs lead to anisotropic physical behaviors different from 3D LHPs, such as strongly confined excitons[15,18] and anisotropic carrier mobility.[23,27] More importantly, the layered structures make the ion diffusion behaviors in RPPs substantially different from those in 3D perovskites and dependent on lattice directions.[28–32] Specifically, the organic spacer cations appear to impede anion diffusion across RPP layers.

Such structural attributes of RPPs have recently enabled the preparation of "vertical" van der Waals heterostructures of RPPs by mechanical stacking[33] or direct growth,[34] but "lateral" heterostructures within the inorganic layers of RPPs are more challenging. Recently, lateral halide heterostructures in 2D $(LA)_2PbX_2$ perovskites (i.e., only $n = 1$) were synthesized by sequentially growing $(LA)_2PbI_4$ epitaxially along the edges of $(LA)_2PbBr_4$ nanosheets.[35] Despite this success,

the complex and dynamic equilibrium between RPPs of different n phases[24,34,36] makes the direct growth of lateral heterostructures of RPPs with $n > 1$ challenging because the second synthesis step could shuffle the pure RPP n phase formed in the first step. An alternative and perhaps more general approach to prepare lateral heterostructures of RPPs could be halide anion exchange starting from various phase-pure RPP phases after they are synthesized, as some earlier reports of post-synthetic modifications of RPP materials using either halide salt vapor or halogen gas suggest that the RPP lattices could be preserved.[37] Contrasting with the isotropic anion exchange well studied in 3D LHPs,[8,9,38-40] the expected anisotropy between ion diffusion along the basal planes versus the out-of-plane direction in RPPs presents much more complexity with many potential controlling variables that remain unexplored. For example, would the quantum well thickness of the RPP phases (the n value) affect the chemical behaviors of anion exchange? This and other structural parameters of RPP also introduce potential opportunities for synthetic control over ionic diffusion to enable heterostructures that demands further systematic study.

Here we show how the layered structures of RPPs affect the morphological outcomes of vapor-solid anion exchange of single-crystal RPP microplates with hydrogen bromide (HBr) vapor to make lateral heterostructures of RPPs. We discover that sharp and stable lateral halide heterojunctions can be formed for a wide range of $n = 1$ and $n = 2$ RPPs because of halide immiscibility; however, diffuse gradient junctions are formed for RPPs with higher n, closer to the ion interdiffusion behaviors in 3D perovskites. We then illustrate how the identities of LA cations and A cations in RPPs can influence their anion exchange behaviors, the kinetics of the anion exchange process, as well as the enhanced stability of the resulted lateral heterostructures, laying the groundwork for post-synthetic preparation of stable lateral heterostructures from arbitrary RPP materials.

RESULTS & DISCUSSION

Vapor-solid anion exchange in Ruddlesden–Popper lead halide perovskites. We first synthesized well-faceted microplates of several RPPs $(LA)_2(A)_{n-1}Pb_nI_{3n+1}$, where LA = n-hexylammonium (HA), n-butylammonium (BA), or phenethylammonium (PEA); A = methylammonium (MA), formamidinium (FA), or guanidinium (GA), via growth from aqueous precursor solution droplets[33,41] or an organic solution dissolution-reprecipitation method (herein referred to as "solution transport")[34,42] (see Experimental and Figure S1 for details). The microplates are tens of microns in lateral dimensions and a few hundred nanometers up to a few micrometers thick (Figure S2). These microplates have well defined shapes and easily identifiable facets suitable for investigating structural influences on anisotropic anion exchange. For brevity, RPP formulas are denoted using the modular notation n = i LA-A-Pb-X, with heterostructures of these materials notated as n = i LA-A-Pb-X/X'. To perform the halide exchange, we exposed these RPP microplates to a controlled flow of HBr vapor at room temperature in a gas flow reactor for specified periods of time (see details in Experimental Section and Figure S3). The H^+ cations are too small to be suitable A-cations in perovskite structures so that HBr will not shift the delicate equilibrium between RP perovskite n phases, and the HBr exchange reaction does not involve redox chemistry.

We found that the layered structure of RPPs makes the anion exchange kinetics substantially faster in the lateral direction along the basal planes of the Pb-X networks than in the vertical out-of-plane direction across the organic LA bilayers (Figure 1a). This is immediately apparent from the color change inward from the edges of the microplates as Br^- replaces I^- in a series of $n = 1$ - 4 HA-MA-Pb-I RPP microplates (Figure 1b-e). There are also fundamental differences among the anion exchange behaviors of different RPP n phases (Figure 1a): $n = 1$ and $n = 2$ microplates display sharp heterojunctions (Figure 1b,c), but gradients of colors are observed toward the edges of $n = 3$ and $n = 4$ microplates (Figure 1d,e).

We further examined this difference using confocal photoluminescence (PL) line scans across the lateral phase boundaries of each I/Br heterostructure (Figure 1f-i). The bromide analogues of each RPP phase have blue-shifted PL due to a composition-dependent bandgap that follows Vegard's law; thus, a continuous change in halide composition across the heterojunction would be expected to result in gradual shifting of a single PL peak as the halide interface is crossed. Instead, $n = 1$ and $n = 2$ RPPs showed an abrupt disappearance of their iodide phase peaks (~525 nm for $n = 1$ in Figure 1f and ~580 nm for $n = 2$ in Figure 1g) with no observable blueshift across the heterojunctions. The 442 nm exciting laser has insufficient energy to excite $n = 1$ & 2 Br RPPs (with expected PL peaks around 410 and 445 nm, respectively), but the lack of peak shifts across these heterostructures (Figure 1f,g) are strong evidence for the discontinuity of the interfaces. In the $n = 2$ case, there is also trace emission from 460-500 nm that corresponds to an emissive defect that is also seen in pure $n = 2$ Br phases (Figure S4c).[43] In contrast, for $n \geq 3$ RPPs, blue-shifting of the original iodide phase peaks were clearly observed across the I/Br interfaces of the heterostructures (Figure 1h-i), which resembles halide mixing observed in 3D LHPs.[39] We used a 532 nm exciting laser for the $n \geq 3$ heterostructures because blue-shifted emission (around 520 nm) from the surface of the microplates dominates the spectra under 442 nm excitation (Figure S5c, e). Nonetheless, the spectra observed under 532 nm excitation confirmed the presence of increasingly bromide-rich phases toward the edges.

The discontinuous interfaces observed in $n \leq 2$ RPPs are a stark contrast to the anion exchange behaviors seen in 3D LHPs, which exhibit halide miscibility under standard conditions.[39,40] We have further confirmed this behavior in these experiments: HBr vapor exchange on $MAPbI_3$ produces 3D halide interfaces that are isotropic and continuous (Figure S6) as a consequence of Fick-like ion diffusion. But even the interfaces of $n \geq 3$ RPP heterostructures show some signs of discrete peak transitions through the individual spectra across the boundaries (Figure S7). This suggests step-wise transitions in halide miscibility between 3D LHPs and RPPs: as the dimensionality of LHPs is reduced from 3D ($n = \infty$) to 2D ($n = 1$), the formation of solid

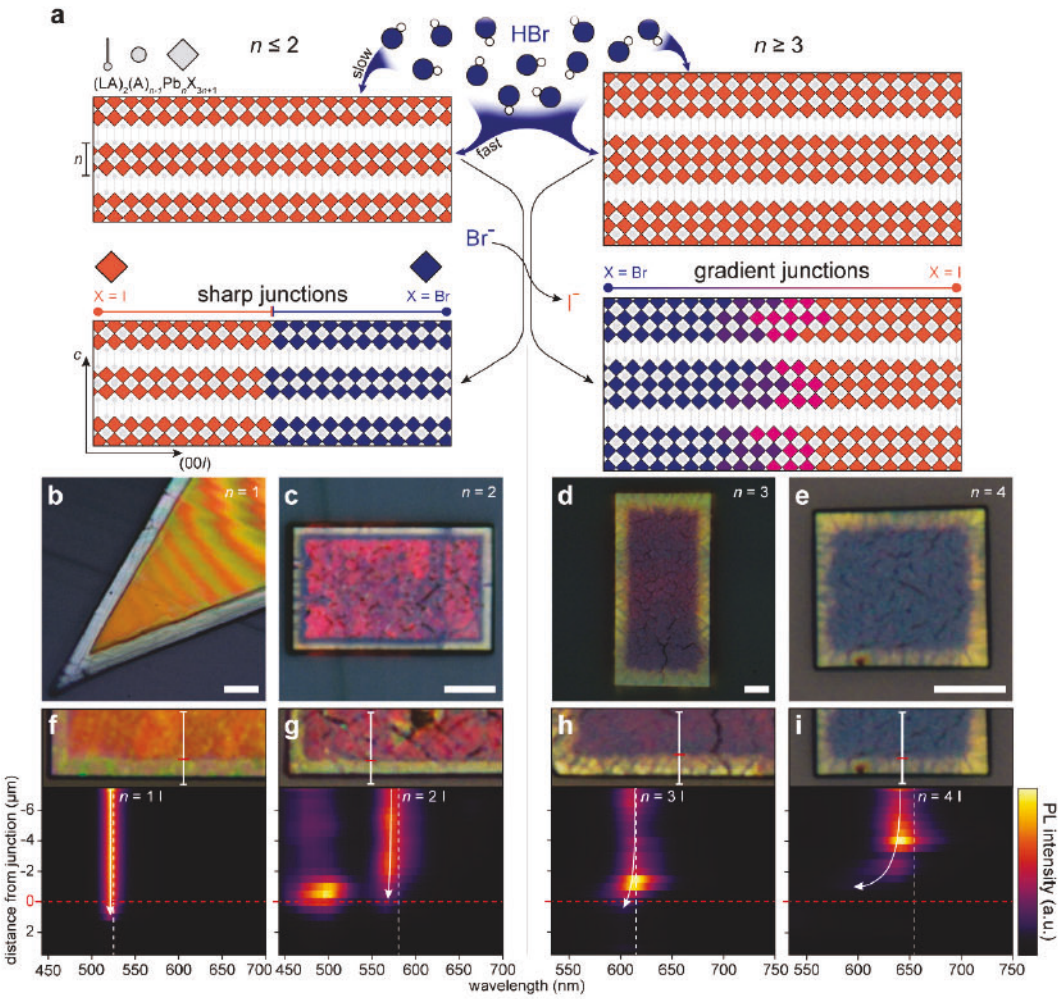

Figure 1. Lateral heterostructures from anion exchange in Ruddlesden-Popper perovskites. (a) Scheme depicting the differing outcomes of vapor-solid anion exchange in lead iodide RPPs using HBr vapor that depend on RPP layer thickness: when n ≤ 2, sharp junctions are formed; when n ≥ 3, gradient junctions are formed. Blue and red diamonds represent $[PbBr_6]^{4-}$ and $[PbI_6]^{4-}$ octahedra, respectively. (b-e) Optical micrographs of representative I/Br heterostructures produced by anion exchange of the homologous series of $(HA)_2(MA)_{n-1}Pb_nI_{3n+1}$ RPPs (n = 1 - 4): (b) $(HA)_2PbI_4$, (c) $(HA)_2(MA)Pb_2I_7$, (d) $(HA)_2(MA)_2Pb_3I_{10}$, (e) $(HA)_2(MA)_3Pb_4I_{13}$. All scale bars are 10 μm. (f-i) PL line scans corresponding to the 12 μm traces on optical images of the heterointerfaces for the corresponding $(HA)_2(MA)_{n-1}Pb_nI_{3n+1}$ RPPs shown above the plots. f & g were collected under 442 nm excitation; h & i were collected under 532 nm excitation. Vertical dashed reference lines indicate the characteristic emission wavelengths for pure $(HA)_2(MA)_{n-1}Pb_nI_{3n+1}$ RPPs. White arrows are visual guides to track wavelength shifts of the peaks as the boundary is crossed.

solutions of mixed halide perovskites becomes increasingly difficult, ultimately arriving at an immiscible, binary phase system (either pure iodide or bromide phases) in the cases of n = 2 and n = 1 RPPs to form heterojunctions with sharp interfaces.

Influence of various cations on anion exchange in Ruddlesden–Popper perovskites. The diverse compositional and structural parameters of RPPs can also influence the anion exchange behaviors. This multi-dimensional RPP phase space can be visualized in Figure 2a using LA cations, A cations, and n value as 3 independent axes. Having revealed the effects of changing n value above (for the specific HA-MA RPPs), we now examine the effects of LA and A cations for the n ≤ 2 RPPs that exhibit sharp heterojunctions.

Three n = 1 $(LA)_2PbI_4$ samples with different LA cations (PEA, BA, HA) show large differences in exchange rates (Figure 2b-d). After 44 h of anion exchange, multiple microns of exchanged bromide phase were visible in the HA microplates (Figure 2d), but no noticeable exchange occurred in the PEA microplates (Figure 2b). The BA microplates had small amounts of exchanged bromide phase present at their edges (Figure 2c), but substantially less than HA microplates. The spacer cations clearly have great influence on the rate of the exchange reactions: the more rigid PEA spacer cations[15] drastically hinder the anion exchange, if permitting it at all (Figure 2e). We hypothesize

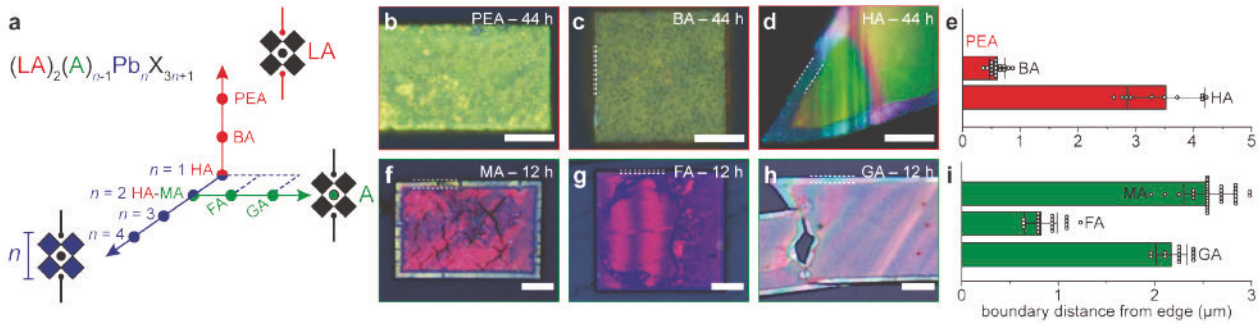

Figure 2. Different anion exchange behaviors in RPPs with various spacer (LA) and A-cations. (a) Pseudo-coordinate mapping of the compositional phase space of lead halide RPPs. (b-d) Optical micrographs of $n = 1$ $(LA)_2PbI_4$ microplates with decreasingly rigid LA spacer cations: (b) PEA, (c) BA, (d) HA, after 44 h of anion exchange with HBr vapor in the same reactor. (f-h) Optical micrographs of $n = 2$ $(HA)_2(A)Pb_2I_7$ RPPs with increasingly large A-site cations: (f) MA, (g) FA, (h) GA, after 12 h of anion exchange with HBr vapor. MA and GA samples were in the same reactor. For b-d and f-h, dashed lines mark the edges and junctions of the resulting heterostructures, and all scale bars are 10 μm. (e, i) Statistics of the boundary propagation distance for various (e) LA spacer cations and (i) A-cations. Error bars represent sample standard deviations. White dots represent individual measurements.

that the rigidity of the interlayer space could affect the permeability of HBr molecules into RPPs. Additionally, anion diffusion must be mediated by structural point defects.[29,44] The rigidity of the LA cation could impact the freedom of structural rearrangements within the Pb-X networks and inhibit the ionic exchange in rigidly templated RPPs (such as those containing PEA).

We further compared the exchange behaviors of $n = 2$ HA-A-Pb-I RPPs with 3 A-site cations of increasing effective radius: MA, FA, and GA.[21,22] After 12 h of exchange, all 3 samples showed noticeable change at the edges (Figure 2f-h). The phase boundaries propagate significantly faster in MA and GA RPPs than in FA RPP (Figure 2i), but the differences in exchange rates among A-cations are less pronounced than those among spacer cations. The resulting lateral heterostructures also displayed different visual quality, with extensive cracking observed across the surfaces of the MA RPP microplates (Figure 2g). This could stem from edge dislocations induced by lattice mismatch at the halide interface, but the exact cause remains unclear. This survey shows that the highest quality lateral RPP heterostructures can be prepared from $n \leq 2$ RPPs containing less rigid spacer cations like HA and A-cations like FA or GA, whereas this vapor-solid exchange method may not yield lateral heterostructures of RPPs containing rigidly packed spacer cations like PEA. These insights can also guide potential direct growth of lateral heterostructures and the previously reported success in sequentially growing lateral heterostructures of $n = 1$ $(LA)_2PbBr_4$ - $(LA)_2PbI_4$[35] is consistent with our findings.

Kinetic characteristics of the anion exchange reaction. These comprehensive findings motivate us to examine the exchange reaction of the $n = 2$ RPP model systems in detail. We visualized the time evolution of the vapor-solid exchange reaction by directly monitoring individual $n = 2$ HA-FA-Pb-I microplates as anion exchange progressed (Figure 3a). At the beginning, the hue uniformly changed across the surface of the microplates, which likely stems from some anion exchange happening on the surface (Figure S8d). After approximately 9 h, the first signs of a grey secondary phase appeared at the edges of the microplates, which then changed in hue to light green until a clearly visible junction formed after approximately 25 h. The junction then propagated inward from the edges, retaining its sharpness throughout. After 81 h, the exchanged bromide rim of the plate with light green color was very prominent and the vertical component of the anion exchange was also sufficiently extensive that the reflected color became dominated by the bromide surface. Interestingly, the structural imperfections in the microplate remained unperturbed as the exchanged phase propagated through them (see Figure S9). Additionally, a control sample of $n = 2$ HA-FA-Pb-I microplates left in the ambient over the same timeframe (Figure 3b and Figure S10) showed extensive degradation, as evidenced by blemishes across the top surface and edges of the microplate. Such contrasting environmental stability suggests that, despite the inevitable presence of moisture in the HBr vapor, the HBr exchange reaction inhibits the normal degradation process in iodide RPPs.

The most remarkable feature of this anion exchange reaction is the retention of the junction's sharpness as it propagates inward. This does not follow Fick's laws of diffusion observed in 3D perovskites[9,39,40] and suggests that a solid-solid interdiffusion mechanism is not at play in $n \leq 2$ RPPs. Instead, we use a simplified gas-solid exchange reaction to model the process:

$$(HA)_2(FA)Pb_2I_7\ (s) + 7\ HBr\ (g) \rightarrow (HA)_2(FA)Pb_2Br_7 + 7\ HI\ (g)$$

with an associated rate law:

$$\frac{d\ (\mathrm{BrRPP})}{dt} = \alpha_{\mathrm{IRPP}}^{a}\alpha_{\mathrm{HBr}}^{b}$$

where α is the activity of each of the species and a and b are the reaction orders for each species. Since the stoichiometric conversion of iodide RPP (IRPP) to bromide RPP (BrRPP) is one-to-one and the associated change in lattice constants is small (according to the reported crystal structures of the BA RPPs[41,43,45]), the propagation of the phase boundary from the plate edge is linearly proportional to the progression of the reaction itself. Thus, we utilize the sharp junction as a "marker plane" to track the reaction

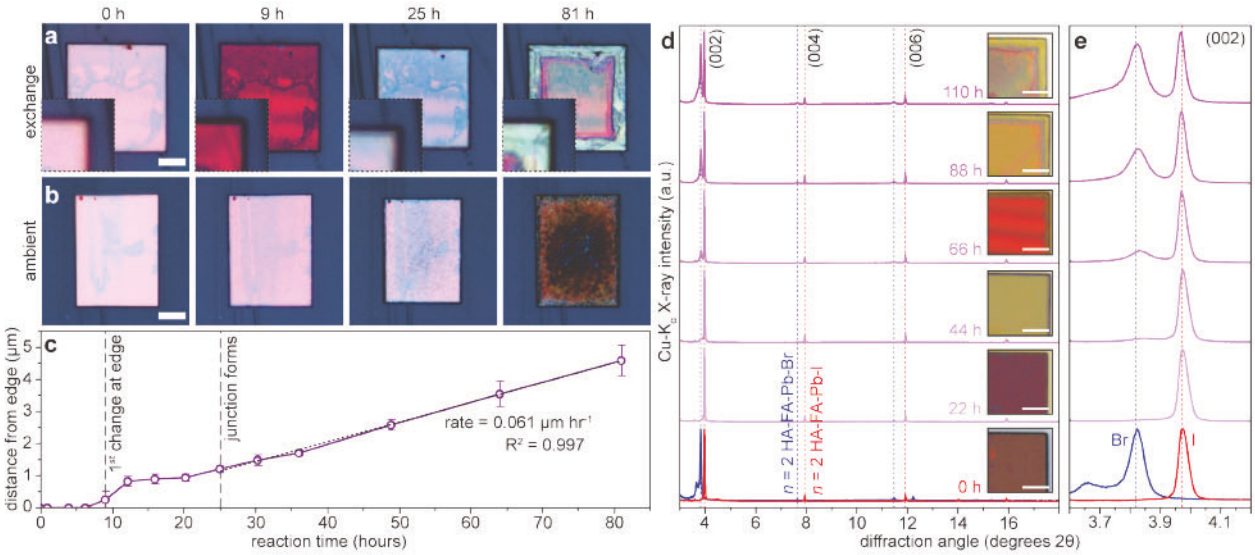

Figure 3. Evolution of anion exchange in $(HA)_2(FA)Pb_2I_7$ microplates. (a, b) Optical micrographs comparing the temporal evolution of two microplates as one (a) underwent anion exchange with HBr vapor and the other (b) was left in ambient environment. (c) Inward propagation of the I–Br lateral phase boundary over time from a sample of microplates undergoing exchange simultaneously with the one shown in **a**. Error bars represent sample standard deviations. The trendline is the linear fit of the time points following pronounced junction formation. (d) PXRD patterns of an $(HA)_2(FA)Pb_2I_7$ microplate sample after undergoing anion exchange for increasing periods of time (from 22 h to 110 h), in comparison to the PXRD patterns of pure $(HA)_2(FA)Pb_2I_7$ and $(HA)_2(FA)Pb_2Br_7$. (e) Detailed view of the evolving (002) reflections from d. The dashed red and blue reference lines correspond to the (00*l*) reflections of pure $(HA)_2(FA)Pb_2I_7$ and $(HA)_2(FA)Pb_2Br_7$, respectively. The inset optical images show the corner of a single microplate in the sample on which XRD analysis was performed. All scale bars are 10 μm. Inset images in (a) are 10 μm × 10 μm.

progress over time in a specific microplate (Figure 3c). The bromide phase did not propagate inward for at least 10 h after it emerged. Following the onset of a visible junction around 25 h, however, the boundary began to propagate linearly with time (Figure 3c), correspondent to a 0th order rate law. The solid RPP has an activity of unity because it is the medium within which the reaction occurs, therefore, a 0th order rate law suggests that a saturation of HBr at the reaction interface must be achieved from the early hours of the exchange reaction.

We also collected X-ray diffraction (XRD) patterns of $(HA)_2(FA)Pb_2I_7$ microplates as they underwent the exchange to elucidate structural changes accompanying the exchange reaction (Figure 3d). Initially, only the (00*l*) reflections of $(HA)_2(FA)Pb_2I_7$ are visible, but after 66 h the equivalent (00*l*) reflections of $(HA)_2(FA)Pb_2Br_7$ emerge in tandem. As the phase boundary begins to propagate inward from the edges of the microplates (Figure 3d insets), the Br:I peak intensity ratio increases (Figure 3e) with no notable peak shifts from either the evolving bromide phase or the iodide starting material. These two discrete iodide and bromide PXRD peak positions, instead of a gradual shift of peak positions, further confirms that mixed I-Br (or alloyed) n = 2 RPP does not form under our exchange conditions. Furthermore, the 0th order reaction kinetics suggests that the halide exchange itself is the rate-limiting step. In 3D LHPs, there is a low thermodynamic barrier to halide substitution, which renders the diffusion of the secondary halides at the surface or within the lattice as the possible the rate-limiting steps, but the results here point to a substantially higher energy barrier to halide mixing in RPPs.

Characterization of sharp lateral heterostructures. We further characterized the resulting highest quality n = 2 HA-FA-Pb-I/Br RPP heterostructures with sharp junctions using (confocal) PL mapping, time-of-flight secondary ion mass spectrometry (ToF-SIMS), and energy dispersive X-ray spectroscopy (SEM-EDS). The binary interface can be clearly seen in the optical and PL micrographs (Figure 4a,b), with no colorimetric shifts in PL across the phase boundary. Confocal PL maps of a heterostructure at the characteristic emission wavelengths of 445 nm for $(HA)_2(FA)Pb_2Br_7$ (Figure 4c) and 580 nm for $(HA)_2(FA)Pb_2I_7$ (Figure 4d) RPPs showed that the two emitting regions are spatially adjacent and non-overlapping, again confirming the compositions of the inner and outer components of the lateral heterostructure as pure single halide phases.

We further used ToF-SIMS to examine both in-plane and out-of-plane composition profiles of this heterostructure (Figure 4e-h). Secondary ion maps of a n = 2 HA-FA-Pb-I/Br microplate confirm the presence of bromide across its entire top surface (Figure 4e), whereas iodide is exclusively present in the center of the microplate (Figure 4f). ToF-SIMS sputtering profiles were collected through the depth

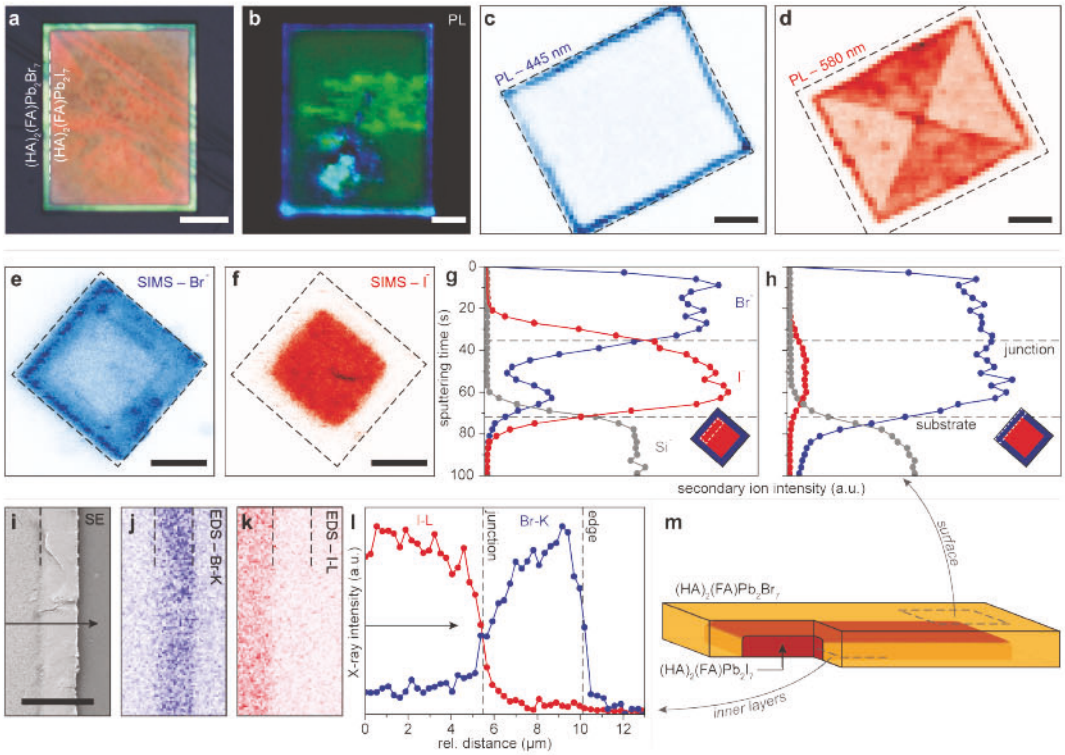

Figure 4. Structural characterization of exchanged lateral heterostructures starting from $(HA)_2(FA)Pb_2I_7$. (a, b) Optical micrographs of representative $n = 2$ HA-FA-Pb-I/Br lateral heterostructures under (a) visible light and (b) 385 nm LED illumination. (c, d) Confocal PL maps of a lateral heterostructure under 442 nm excitation within the characteristic emission regions for (c) $n = 2$ Br (445 nm) and (d) $n = 2$ I RPPs (580 nm). (e, f) ToF-SIMS halide maps of a lateral heterostructure showing (e) bromide and (f) iodide signal intensities. Dashed outlines in c-f represent the spatial footprints of the microplate. (g, h) SIMS sputtering profiles collected at the (g) inner and (h) outer components of the heterostructure imaged in e and f. Inset cartoons indicate the sputtering areas as dashed boxes. (i) Top-down SEM image of an exfoliated layer of a lateral heterostructure with the corresponding halide EDS maps at (j) Br-K and (k) I-L characteristic X-Ray energies. (l) EDS line scan corresponding to the arrow in i. (m) Illustration of the 3D morphology of an exchanged $n = 2$ HA-FA-Pb-I/Br heterostructure showing a cross section. The vertical dimension is disproportionately large in scale to emphasize detail. All scale bars are 10 μm.

of the heterostructure. The center profile (Figure 4g) shows that the upper fraction of the microplate contains only bromide, with an increase of iodide and decrease of bromide concentration beginning approximately one third into the total depth of the plate. The edge sputtering profile (Figure 4h), however, is dominated by bromide throughout the entire depth of the plate. EDS mapping performed on a heterostructure after the top layer was exfoliated (Figure 4j-l) eliminated the convolution from the bromide-rich top surface. The EDS maps confirm the sharp lateral interface, and the EDS line scan across the same interface (Figure 4l) shows a transition from I to Br over a distance of ~2 μm, setting an upper limit to the diffuseness of the heterojunction. We were unable to measure the height of the specific microplate studied with ToF-SIMS but based on atomic force microscopy (AFM) measurements and optical imaging of similar $n = 2$ HA-FA-Pb-I/Br lateral heterostructures (Figure S11), we can estimate a lateral anion exchange distance exceeding an order of magnitude greater than the possible vertical exchange depth, which is limited to the height of the microplate (see additional discussion associated with Figure S11). These results suggest a core-shell "3D" heterostructure morphology with an overwhelming lateral bias, as illustrated in Figure 4m. An important consequence of the non-zero vertical anion exchange is that top-down exchange could dominate over lateral exchange in exceedingly thin nanosheets (see an example in Figure S8d), presenting a potential method to completely exchange the halide ions of some RPP starting materials with spatial control using patterned masks.

Stability of lateral RPP heterostructures. Finally, these lateral RPP heterostructures with sharp interfaces formed by anion exchange are more stable against anion interdiffusion and degradation. Again using $n = 2$ HA-FA-Pb-I/Br heterostructures as a model system, we first assessed the effects of temperature by heating two separate lateral heterostructure samples in an oven for 12 h at temperatures of 50 and 100 °C (Figure 5a-c). Surprisingly, the boundary between the iodide and bromide phases remained sharp even under elevated temperatures of 50 °C (Figure 5b), which is harsher than the operating conditions of many optoelectronic devices, and there was no noticeable sign of general degradation in comparison with the starting microplates (Figure 5a). Even at 100 °C (Figure 5c), the phase boundary remained mostly intact, but there was extensive warping and striations across the microplate, suggesting that the interdiffusion threshold of the junction is comparable to the structural degradation threshold of the RPP materials.

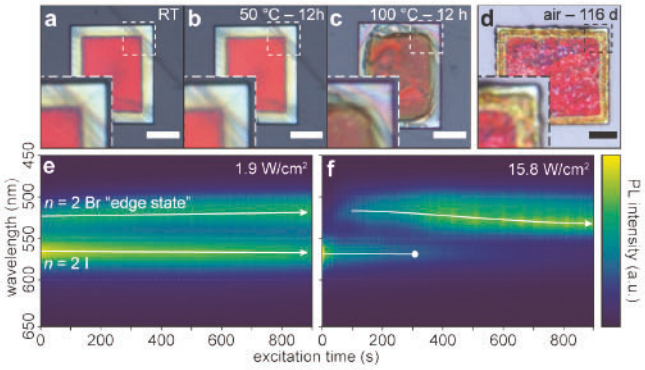

Figure 5. Stability of lateral RPP heterostructures after anion exchange from $(HA)_2(FA)Pb_2I_7$. (a-c) Optical micrographs $n = 2$ HA-FA-Pb-I/Br lateral heterostructures after being held at increasing temperatures for extended periods: (a) room temperature at the start, (b) at 50 °C for 12 h, (c) at 100 °C for 12 h. (d) Optical micrograph of an $n = 2$ HA-FA-Pb-I/Br lateral heterostructure left in desiccated air for 116 d. Bottom-left insets in a-d show magnified 10 × 10 μm corner regions highlighted in the corresponding micrographs with dashed boxes. All scale bars are 10 μm. (e, f) Temporal evolution of PL spectra from an exfoliated junction of an $n = 2$ HA-FA-Pb-I/Br lateral heterostructure under confocal 442 nm CW excitation at (e) low (1.9 W/cm²) and (f) high irradiance (15.8 W/cm²). White arrows are visual guides to track spectral shifts and feature onsets over time.

We also kept an unencapsulated sample of these heterostructures in a sealed petri dish with desiccant for 116 days to evaluate environmental stability (Figure 5d). There was some surface degradation as evidenced by spot-like blemishes, but even after 116 days, the basic lateral heterostructure morphology retained and the microplate had not yet degraded to the extent that the starting $(HA)_2FAPb_2I_7$ microplates did in under 100 h under ambient conditions (Figure 3b). The junction of the pictured specimen showed a third yellow-colored band toward the edges of the microplate. PL line scans of an analogous ternary junction after exfoliation (Figure S5h) showed that the new feature was likely a mixed halide phase, suggesting that some ion interdiffusion may have eventually occurred over such an extended duration.

Photoinduced ion diffusion is also a significant source of degradation for halide perovskite heterojunctions.[13] We focused a 442 nm CW laser onto the junction of an exfoliated layer of the lateral heterostructure and monitored PL spectral changes over the course of the 15 min excitation period. Under lower laser irradiance (1.9 W/cm², ~18 suns' equivalent) the spectra remained the same throughout (Figure 5e), but under much more intense irradiance (15.8 W/cm², ~150 suns' equivalent) significant spectral changes were observed (Figure 5f): the intensity of the characteristic $n = 2$ I emission peak at 580 nm significantly diminished. Concurrently, the 525 nm peak associated with a Br RPP edge state[43] began to intensify and red-shift, indicating that the junction was changing over time. Inspection of the microplate after the experiment revealed no significant physical damage, suggesting that the PL spectral changes were likely caused by compositional changes induced by the excitation.

These results show that these lateral halide heterojunctions of RPPs are much more stable than the halide junctions in 3D LHPs in that they display dramatically suppressed anion interdiffusion (but not eliminating it) along both basal plane and out-of-plane directions. Additionally, the enhanced environmental resilience of the RPP heterostructures compared to starting lead iodide RPP materials suggests that the bromide-rich RPP surfaces are more robust, making anion exchange a convenient approach for stabilizing iodide RPP surfaces.

CONCLUSIONS

We have shown that the anisotropic anion exchange behaviors in RPPs substantially and systematically differ from those in 3D LHPs as a function of decreasing perovskite layer thickness due to increasing halide immiscibility in these 2D structures. These attributes enable the formation of sharp halide lateral heterostructures of $n = 1$ and 2 RPP phases via anion exchange. In contrast, RPPs with $n \geq 3$ form more diffuse compositional gradients upon anion exchange. Furthermore, the anion exchange behaviors can be fine-tuned by the structural characteristics of the LA spacer and A-site cations. The findings from our systematic exploration of anion exchange in RPPs enabled the preparation of high-quality lateral heterostructures of $n = 2$ RPPs that are more stable against anion interdiffusion and degradation than similar interfaces in 3D perovskites and suitable for the operating environments of many optoelectronic devices. This study provides new insights on the complex, anisotropic halide diffusion behaviors of RPPs and demonstrates the capacity of anion exchange as a general post-synthetic modification technique to prepare stable lateral heterostructures from existing RPP starting materials to enable their future optoelectronic device applications.

EXPERIMENTAL SECTION

Chemicals and materials. All chemicals were used as purchased without further purification. Lead(II) iodide (PbI_2, 99.999%), lead(II) acetate trihydrate ($Pb(CH_3COO)_2 \bullet 3\ H_2O$, 99%), and hypophosphorous acid solution (H_3PO_2, 50 wt. % in H_2O) were purchased from Sigma Aldrich. Concentrated hydrobromic acid (HBr, 48 wt. % in H_2O), concentrated hydroiodic acid (HI, 55-58 wt. % in H_2O), and lead(II) bromide ($PbBr_2$, 98+%) were purchased from Alfa Aesar. Methylammonium iodide (MAI), formamidinium iodide (FAI), formamidinum bromide (FABr), guanidinium iodide (GAI), phenethylammonium iodide (PEAI), *n*-butylammonium iodide (BAI), *n*-hexylammonium iodide (HAI), and *n*-hexylammonium bromide (HABr) were purchased from GreatCell Solar. Isopropanol (IPA, 99%) was purchased from Fisher Scientific. 5 mil fluorinated ethylene propylene (FEP) film was wiped with IPA prior to use in synthesis. Silicon substrates [n-type, (111)] with 100 nm native oxide were cleaned with methanol using delicate task wipes prior to use in synthesis.

Aqueous droplet growth of RPP microplates. All synthesis was carried out in ambient conditions. 1 M stock precursor solutions of PbI_2 and the various organoammonium

iodide salts were prepared by dissolving the precursor salts in a 10:1 (by volume) solution of HI and H_3PO_2. To synthesize a given RPP compositional target $(LA)_2(A)_{n-1}Pb_nI_{3n+1}$, the 1 M HI solutions of (LA)I, AI, and PbI_2 were mixed in a specific ratio (see Table S1) and heated in a scintillation vial to ~110 °C until all precipitate was dissolved. They were then transferred to a polypropylene centrifuge tube and cooled to room temperature, and then precisely heated to the appropriate supersaturation temperature in a PCR thermal cycler (Abbott LCx) (see Table S1) and held there for >1 h to equilibrate. Meanwhile, a glass microscope slide was placed bridged over a glass petri dish to make the stage and the catch pan for the reaction, respectively (see Figure S1a). A small (~1 cm × 2 cm) strip of FEP film was placed level on the reaction stage, which was then placed under a reflective optical microscope (Olympus BX51) with a high working distance objective lens and brought into focus. The equilibrated stock solution was removed from the thermal cycler and a large drop of the reaction mixture (without any solids) was pipetted out within 30 s and carefully dispensed onto the center of the FEP substrate at room temperature (Figure S1a). The growth of the microplates was monitored live using the microscope. Once the desired average crystal size was reached, usually 50-100 μm along one side, the FEP substrate was tilted over the edge of the slide with tweezers, allowing the large droplet to roll off the hydrophobic FEP substrate into the petri dish. The substrate was then quickly placed under a moderate flow of nitrogen gas for ~10 s to blow off remaining solution droplets, leaving a dry substrate with a population of tens to hundreds of RPP microplates. The same approach was taken to synthesize $(HA)_2(FA)Pb_2Br_7$ with the bromide analogues of each compound in a 10:1 (by volume) solution of HBr and H_3PO_2. The phase purity of the samples was verified using powder XRD and confocal PL measurements of a large population of the microplates in a sample (Figures S11 & S12).

Solution transport growth of $(HA)_2(FA)Pb_2I_7$ microplates. An organoammonium precursor mixture of 10 mM HAI and 295 mM FAI in IPA was prepared quantitatively with volumetric glassware. Following the general approach previously reported,[42] a lead acetate film was prepared by casting a few drops of a methanol solution of 100 mg/mL $Pb(CH_3COO)_2 \bullet 3\ H_2O$ across the surface of a 1 cm² glass microscope slide and drying it on a hot plate at 80 °C for about 30 min. In a 4-dram (~15 mL) glass vial, a 1 cm² piece of Si/SiO_2 substrate was placed with its polished side up into 2 mL of the precursor mixture. The lead acetate covered glass slide was then gently placed film side down onto the silicon substrate, such that the surface area in mutual contact was maximized (Figure S1b). They were then allowed to sit for 90 h at room temperature before being carefully and gently removed from the vials with tweezers. The silicon substrate was washed gently in an IPA bath and dried under a stream of nitrogen gas and repeated one more time to remove the organic precursor residue prior to storage (Figure S1c). The exchange behavior of $(HA)_2(FA)Pb_2I_7$ microplates prepared with this method is qualitatively similar to that of $(HA)_2(FA)Pb_2I_7$ microplates prepared via aqueous droplet growth (Figure S14).

Vapor-solid anion exchange reactions. The vapor-solid anion exchange reactions were performed by exposing a RPP sample in a reaction chamber at room temperature to a continuous flow of hydrogen bromide (HBr) vapor made by bubbling nitrogen gas through a concentrated HBr solution (48 wt. %). As illustrated in Figure S2, the exchange reactor was assembled in a fume hood consisting of, in order of flow direction, a gas flow regulator, a gas washing bottle filled with 75 mL of concentrated HBr, a drying tube packed with 10 g of indicator-free 8 mesh Drierite® desiccant between two wads of glass wool, a coarse frit glass filtration funnel sealed with a stemmed rubber stopper (serving as a sample chamber), and a filtration flask containing saturated sodium bicarbonate solution and sealed with a stemmed rubber stopper. The entire apparatus was connected with Tygon® tubing and all glass fittings were sealed with silicone vacuum grease. The substrates covered with microplates of various RPPs were placed in the sample chamber and the anion exchange reaction was typically run at a nitrogen gas flow rate of 0.4 standard liters per minute (SLM) for the desired amount of time, with desiccant being replaced after every ~24 h of reaction time.

Preparation of exfoliated heterostructure layers from large $(HA)_2(FA)Pb_2I_7$ crystals. The same $(HA)_2(FA)Pb_2I_7$ reaction mixture that was used for aqueous droplet growth was heated at 75 °C for 3 h before cooling to room temperature at 1 °C/h to promote the slow growth of large crystals. The resulting crystals were vacuum filtered, washed with ~ 5 mL of chilled diethyl ether and dried under vacuum overnight. The crystals were subjected to anion exchange for 24 h (see above) and then mechanically exfoliated using scotch tape. The exfoliation process was repeated a few times until the exfoliated crystal flakes appeared translucent under a microscope. The flakes were then transferred to a silicon substrate by lightly laminating the tape onto the substrate and slowly peeling off multiple times in sections.

Optical and (confocal) photoluminescence microscopy. Optical micrographs were collected using an Olympus BX51 widefield microscope configured in a reflective geometry. Images were captured using Spot Insight 2 or ThorLabs Kiralux CS895CU CMOS cameras. Objective lens scales were calibrated prior to boundary propagation length measurements using the standard elements of a USAF 1951 resolution test target (ThorLabs). PL micrographs were collected using the same microscope under the direct illumination from an Infray pen light handheld 385 nm LED flashlight. A 427 nm longpass filter was placed along the optic axis of the microscope to filter out the incident light. PL images were captured using a Sony Alpha a6000 digital camera with long exposures (>5 s) and low gain (ISO100). Confocal PL maps and line scans were acquired using a Horiba Labram Aramis confocal Raman/photoluminescence microscope with a Horiba Synapse CCD detector and a motorized XYZ stage under 442 nm or 532 nm CW laser excitation. For line scans, an 1800 groove/mm grating was used. A 300 groove/mm grating was used for mapping acquisitions. The gratings were calibrated to the 520.7 cm^{-1} Raman line of silicon under excitation from a 532 nm CW laser. A 100× microscope objective was used for mapping acquisitions, with approximate spot sizes (FWHM) of 1 μm (442 nm) and 4 μm (532 nm).

Time-resolved photoluminescence spectroscopy. Steady state and time-resolved PL measurements were

performed using a custom-built TRPL microscope. The 800 nm fundamental of a mode-locked Ti:sapphire oscillator (Coherent Vitesse, 80 MHz rep. rate, 100 fs pulse duration) was frequency doubled to 400 nm using a crystal of barium borate (BBO) and focused onto the sample through a 100× microscope objective. The emitted light was then collected through the same objective and sent into a spectrograph (Princeton Instruments Acton SP2300i), where it was dispersed with a 150 g/mm grating onto a sCMOS camera (Andor Neo) for spectra, or an avalanche photodiode (IQD ID-100) coupled to a time-correlated single photon counting module (Becker & Hickl SPC-130) for transients. All measurements were conducted at pulse fluence of 2.37 μJ/cm2.

Time-of-flight secondary ion mass spectrometry. The $(HA)_2(FA)Pb_2I_7$ microplate samples used for ToF-SIMS analysis were grown directly on a n-type silicon substrate via the solution transport growth (to prevent charging during analysis) followed by the anion exchange reaction as described above. ToF-SIMS measurements were performed using a TOF-SIMS5 instrument (IONTOF GmbH, Münster, Germany) with dual beam non-interlaced mode depth profiling at the Environmental Molecular Sciences Laboratory (EMSL) of Pacific Northwest National Laboratory. A 2.0 keV Cs^+ beam was used as the sputtering beam and a 25 keV Bi^+ beam was used as the analysis beam for ion image collection. The Cs^+ sputtering beam (~140 nA) was scanned over a 200×200 μm² area. The Bi^+ beam was focused to be about 0.40 μm in diameter with a beam current of about 1.20 pA at a 20 kHz frequency. During image collection, the Bi^+ beam was scanned with 256×256 pixels over an area of 70×70 μm² at the Cs^+ sputter crater center. The non-interlaced mode was operated at 3.0 s sputtering time, 1.0 s pause time and 6.55 s data collection time (2 scans of 256×256 pixels). A low energy (10 eV) electron flood gun was used for charge compensation in all measurements. Data reconstruction was performed to get digital zoom-in ion maps and depth profiles of interesting ion species at desirable areas. The complete SIMS sputtering profiles for all species are shown in Figure S15.

Scanning electron microscopy and energy dispersive X-Ray spectroscopy. Intact microplates imaged via SEM were directly grown on Si substrates via the solution transport growth. The heterostructure subjected to EDS analysis in Figure 4i-j was from a large crystal grown from aqueous solution and exfoliated as described above. Scanning electron micrographs were collected using a Carl Zeiss LEO Supra 55V field emission SEM at an accelerating voltage of 3 kV. EDS analysis was performed in the same SEM at an accelerating voltage of 25 kV and a working distance of 8 ± 0.1 mm, for which the Si drift EDS detector was calibrated. EDS maps were acquired with a signal continuously summated over a 600 s acquisition. For EDS line scans, 100-point lines were used and summated thrice per acquisition, with a dwell time of 0.5 s/point.

Other structural characterizations. Powder X-ray diffraction patterns were collected using a Bruker D8 Advance powder X-ray diffractometer with the Cu-K_α line. A knife edge was used to attenuate incident X-ray background at low diffraction angles. AFM topography measurements were performed using an Agilent Keysight 5500 atomic force microscope in tapping mode with a Bruker NCHV-A tip (spring constant: 40 N m^{-1}).

Optical tracking of heterostructure phase boundary propagation. Two samples of $(HA)_2(FA)Pb_2I_7$ microplates on FEP films prepared via aqueous droplet growth were imaged immediately prior to the experiment under consistent exposure time and sensor gain. One sample was subjected to the exchange reaction while a control sample was left out in ambient environment. The samples were periodically imaged under the microscope at chosen time points. At certain time intervals, the samples were stored overnight between time points in a sealed desiccator in the dark. The microplates were imaged before and after overnight cycles to ensure no changes had occurred beyond the controlled reactions themselves. The boundary propagation distance was measured using ImageJ image analysis software by aligning image sequences of each individual microplate in time series. The junctions and edges are local minima in pixel intensity, which are reliable gauges to track. The distances were measured in integer numbers of pixels with no subpixel interpolation, instead relying on the statistics of all edge measurements made in the sample to determine the measurement uncertainty. Each side of each quadrilateral microplate served as a measurement point, with measurement lines bisecting each microplate edge.

Temperature and temporal stability experiments. A sample of n = 2 HA-FA-Pb-I/Br heterostructures and n = 2 HA-FA-Pb-I microplates inside a covered, desiccated glass Petri dish were placed inside a temperature-controlled oven at 50 °C for 12 h. The same process was performed on a second sample at 100 °C. A control sample in a desiccated container outside the oven was left in the dark under ambient environment while the test samples were in the oven. A sample of n = 2 HA-FA-Pb-I/Br heterostructures grown via aqueous droplet growth was left inside a sealed, desiccated polystyrene Petri dish for 116 days in the dark before being removed for imaging.

Photostability experiment. Time-dependent confocal PL spectra were collected using a Horiba Labram Aramis confocal Raman/photoluminescence microscope. A freshly exfoliated layer of an n = 2 HA-FA-Pb-I/Br heterostructure (see above) was continuously excited with a 442 nm CW laser, which was passed through two different neutral density filters and focused onto the junction with a 50× objective lens. Irradiances were calculated using power measurements from a photodiode power meter (ThorLabs S120VC) and the spot sizes (FWHM) from microscope images taken during the experiment. The PL spectra were collected at 10 s (low irradiance) and 15 s (high irradiance) intervals for 15 min each using an 1800 groove/mm grating. Each trial was done at separate spots on the same exfoliated heterostructure plate to avoid convolving the two outcomes.

ASSOCIATED CONTENT

Supporting Information.

Additional experimental details, schemes, and safety notes; synthetic parameters for compounds studied in the main text; microplate morphology characteristics; additional PL line scans; examples of exchange on 3D LHPs with HBr vapor; spectral decompositions of PL line scans; full image matrices for the exchange kinetics study; AFM topography measurements of

microplates; XRD patterns of the compounds studied in the main text.
This material is available free of charge via the Internet at http://pubs.acs.org.

AUTHOR INFORMATION

Corresponding Author

Song Jin – *Department of Chemistry, University of Wisconsin – Madison, 1101 University Avenue, Madison, Wisconsin 53706, United States*
http://orcid.org/0000-0001-8693-7010; Email: jin@chem.wisc.edu

Authors

Chris R. Roy – *Department of Chemistry, University of Wisconsin – Madison, 1101 University Avenue, Madison, Wisconsin 53706, United States*

https://orcid.org/0000-0001-6438-9543

Dongxu Pan – *Department of Chemistry, University of Wisconsin – Madison, 1101 University Avenue, Madison, Wisconsin 53706, United States*

https://orcid.org/0000-0002-4437-5459

Yining Wang – *Environmental Molecular Sciences Laboratory, Pacific Northwest National Laboratory, 902 Battelle Boulevard, Richland, Washington 99352, United States*

Matthew P. Hautzinger – *Department of Chemistry, University of Wisconsin – Madison, 1101 University Avenue, Madison, Wisconsin 53706, United States*

https://orcid.org/0000-0002-4764-3076

Yuzhou Zhao – *Department of Chemistry, University of Wisconsin – Madison, 1101 University Avenue, Madison, Wisconsin 53706, United States*

https://orcid.org/0000-0002-1610-8273

John C. Wright – *Department of Chemistry, University of Wisconsin – Madison, 1101 University Avenue, Madison, Wisconsin 53706, United States*

https://orcid.org/0000-0002-6926-1837

Zihua Zhu – *Environmental Molecular Sciences Laboratory, Pacific Northwest National Laboratory, 902 Battelle Boulevard, Richland, Washington 99352, United States*

https://orcid.org/0000-0001-5770-8462

Notes

The authors declare no competing interests.

ACKNOWLEDGMENTS

This work is supported by the Department of Energy, Office of Basic Energy Sciences, Division of Materials Sciences and Engineering, under Award DE-FG02-09ER46664. The authors acknowledge use of facilities and instrumentation supported by the NSF through the University of Wisconsin Materials Research Science and Engineering Centre (DMR-1720415). The SIMS experiments were performed at EMSL, a DOE Office of Science User Facility sponsored by the Biological and Environmental Research program.

REFERENCES

(1) Stranks, S. D.; Snaith, H. J. Metal-Halide Perovskites for Photovoltaic and Light-Emitting Devices. *Nature Nanotechnology* **2015**, *10* (5), 391–402.

(2) Zhu, H.; Fu, Y.; Meng, F.; Wu, X.; Gong, Z.; Ding, Q.; Gustafsson, M. V.; Trinh, M. T.; Jin, S.; Zhu, X.-Y. Lead Halide Perovskite Nanowire Lasers with Low Lasing Thresholds and High Quality Factors. *Nature Materials* **2015**, *14* (6), 636–642.

(3) Fu, Y.; Zhu, H.; Chen, J.; Hautzinger, M. P.; Zhu, X.-Y.; Jin, S. Metal Halide Perovskite Nanostructures for Optoelectronic Applications and the Study of Physical Properties. *Nature Reviews Materials* **2019**, *4* (3), 169–188.

(4) Yin, W.-J.; Shi, T.; Yan, Y. Unusual Defect Physics in CH3NH3PbI3 Perovskite Solar Cell Absorber. *Appl. Phys. Lett.* **2014**, *104* (6), 063903.

(5) Manser, J. S.; Christians, J. A.; Kamat, P. V. Intriguing Optoelectronic Properties of Metal Halide Perovskites. *Chem. Rev.* **2016**, *116* (21), 12956–13008.

(6) Protesescu, L.; Yakunin, S.; Bodnarchuk, M. I.; Krieg, F.; Caputo, R.; Hendon, C. H.; Yang, R. X.; Walsh, A.; Kovalenko, M. V. Nanocrystals of Cesium Lead Halide Perovskites (CsPbX3, X = Cl, Br, and I): Novel Optoelectronic Materials Showing Bright Emission with Wide Color Gamut. *Nano Lett.* **2015**, *15* (6), 3692–3696.

(7) Alferov, Zh. I. The History and Future of Semiconductor Heterostructures. *Semiconductors* **1998**, *32* (1), 1–14.

(8) Dou, L.; Lai, M.; Kley, C. S.; Yang, Y.; Bischak, C. G.; Zhang, D.; Eaton, S. W.; Ginsberg, N. S.; Yang, P. Spatially Resolved Multicolor $CsPbX_3$ Nanowire Heterojunctions via Anion Exchange. *Proc Natl Acad Sci USA* **2017**, *114* (28), 7216.

(9) Pan, D.; Fu, Y.; Chen, J.; Czech, K. J.; Wright, J. C.; Jin, S. Visualization and Studies of Ion-Diffusion Kinetics in Cesium Lead Bromide Perovskite Nanowires. *Nano Lett.* **2018**, *18* (3), 1807–1813.

(10) Scheidt, R. A.; Kamat, P. V. Temperature-Driven Anion Migration in Gradient Halide Perovskites. *J. Chem. Phys.* **2019**, *151* (13), 134703.

(11) Hoke, E. T.; Slotcavage, D. J.; Dohner, E. R.; Bowring, A. R.; Karunadasa, H. I.; McGehee, M. D. Reversible Photo-Induced Trap Formation in Mixed-Halide Hybrid Perovskites for Photovoltaics. *Chem. Sci.* **2015**, *6* (1), 613–617.

(12) Draguta, S.; Sharia, O.; Yoon, S. J.; Brennan, M. C.; Morozov, Y. V.; Manser, J. S.; Kamat, P. V.; Schneider, W. F.; Kuno, M. Rationalizing the Light-Induced Phase Separation of Mixed Halide Organic–Inorganic Perovskites. *Nature Communications* **2017**, *8* (1), 200.

(13) Bischak, C. G.; Hetherington, C. L.; Wu, H.; Aloni, S.; Ogletree, D. F.; Limmer, D. T.; Ginsberg, N. S. Origin of Reversible Photoinduced Phase Separation in Hybrid Perovskites. *Nano Lett.* **2017**, *17* (2), 1028–1033.

(14) Wang, Y.; Chen, Z.; Deschler, F.; Sun, X.; Lu, T.-M.; Wertz, E. A.; Hu, J.-M.; Shi, J. Epitaxial Halide Perovskite Lateral Double Heterostructure. *ACS Nano* **2017**, *11* (3), 3355–3364.

(15) Blancon, J.-C.; Even, J.; Stoumpos, Costas. C.; Kanatzidis, Mercouri. G.; Mohite, A. D. Semiconductor Physics of Organic–Inorganic 2D Halide Perovskites. *Nature Nanotechnology* **2020**, *15* (12), 969–985.

(16) Smith, I. C.; Hoke, E. T.; Solis-Ibarra, D.; McGehee, M. D.; Karunadasa, H. I. A Layered Hybrid Perovskite Solar-Cell Absorber with Enhanced Moisture Stability. *Angewandte Chemie International Edition* **2014**, *53* (42), 11232–11235.

(17) Spitha, N.; Kohler, D. D.; Hautzinger, M. P.; Li, J.; Jin, S.; Wright, J. C. Discerning between Exciton and Free-Carrier Behaviors in Ruddlesden–Popper Perovskite Quantum Wells through Kinetic Modeling of Photoluminescence Dynamics. *J. Phys. Chem. C* **2020**, *124* (31), 17430–17439.

(18) Katan, C.; Mercier, N.; Even, J. Quantum and Dielectric Confinement Effects in Lower-Dimensional Hybrid Perovskite Semiconductors. *Chem. Rev.* **2019**, *119* (5), 3140–3192.

(19) Saparov, B.; Mitzi, D. B. Organic–Inorganic Perovskites: Structural Versatility for Functional Materials Design. *Chem. Rev.* **2016**, *116* (7), 4558–4596.

(20) Gao, Y.; Shi, E.; Deng, S.; Shiring, S. B.; Snaider, J. M.; Liang, C.; Yuan, B.; Song, R.; Janke, S. M.; Liebman-Peláez, A.; Yoo, P.; Zeller, M.; Boudouris, B. W.; Liao, P.; Zhu, C.; Blum, V.; Yu, Y.; Savoie, B. M.; Huang, L.; Dou, L. Molecular Engineering of Organic–Inorganic Hybrid Perovskites Quantum Wells. *Nature Chemistry* **2019**, *11* (12), 1151–1157.

(21) Fu, Y.; Hautzinger, M. P.; Luo, Z.; Wang, F.; Pan, D.; Aristov, M. M.; Guzei, I. A.; Pan, A.; Zhu, X.; Jin, S. Incorporating Large A Cations into Lead Iodide Perovskite Cages: Relaxed Goldschmidt Tolerance Factor and Impact on Exciton–Phonon Interaction. *ACS Cent. Sci.* **2019**, *5* (8), 1377–1386.

(22) Hautzinger, M. P.; Pan, D.; Pigg, A. K.; Fu, Y.; Morrow, D. J.; Leng, M.; Kuo, M.-Y.; Spitha, N.; Lafayette, D. P.; Kohler, D. D.; Wright, J. C.; Jin, S. Band Edge Tuning of Two-Dimensional Ruddlesden–Popper Perovskites by A Cation Size Revealed through Nanoplates. *ACS Energy Lett.* **2020**, *5* (5), 1430–1437.

(23) Tsai, H.; Nie, W.; Blancon, J.-C.; Stoumpos, C. C.; Asadpour, R.; Harutyunyan, B.; Neukirch, A. J.; Verduzco, R.; Crochet, J. J.; Tretiak, S.; Pedesseau, L.; Even, J.; Alam, M. A.; Gupta, G.; Lou, J.; Ajayan, P. M.; Bedzyk, M. J.; Kanatzidis, M. G.; Mohite, A. D. High-Efficiency Two-Dimensional Ruddlesden–Popper Perovskite Solar Cells. *Nature* **2016**, *536* (7616), 312–316.

(24) Yuan, M.; Quan, L. N.; Comin, R.; Walters, G.; Sabatini, R.; Voznyy, O.; Hoogland, S.; Zhao, Y.; Beauregard, E. M.; Kanjanaboos, P.; Lu, Z.; Kim, D. H.; Sargent, E. H. Perovskite Energy Funnels for Efficient Light-Emitting Diodes. *Nature Nanotechnology* **2016**, *11* (10), 872–877.

(25) Liang, D.; Peng, Y.; Fu, Y.; Shearer, M. J.; Zhang, J.; Zhai, J.; Zhang, Y.; Hamers, R. J.; Andrew, T. L.; Jin, S. Color-Pure Violet-Light-Emitting Diodes Based on Layered Lead Halide Perovskite Nanoplates. *ACS Nano* **2016**, *10* (7), 6897–6904.

(26) Zhang, F.; Lu, H.; Tong, J.; Berry, J. J.; Beard, M. C.; Zhu, K. Advances in Two-Dimensional Organic–Inorganic Hybrid Perovskites. *Energy Environ. Sci.* **2020**, *13* (4), 1154–1186.

(27) Liu, Y.; Ye, H.; Zhang, Y.; Zhao, K.; Yang, Z.; Yuan, Y.; Wu, H.; Zhao, G.; Yang, Z.; Tang, J.; Xu, Z.; Liu, S. (Frank). Surface-Tension-Controlled Crystallization for High-Quality 2D Perovskite Single Crystals for Ultrahigh Photodetection. *Matter* **2019**, *1* (2), 465–480.

(28) Lin, Y.; Bai, Y.; Fang, Y.; Wang, Q.; Deng, Y.; Huang, J. Suppressed Ion Migration in Low-Dimensional Perovskites. *ACS Energy Lett.* **2017**, *2* (7), 1571–1572.

(29) Xiao, X.; Dai, J.; Fang, Y.; Zhao, J.; Zheng, X.; Tang, S.; Rudd, P. N.; Zeng, X. C.; Huang, J. Suppressed Ion Migration along the In-Plane Direction in Layered Perovskites. *ACS Energy Lett.* **2018**, *3* (3), 684–688.

(30) Huang, Z.; Proppe, A. H.; Tan, H.; Saidaminov, M. I.; Tan, F.; Mei, A.; Tan, C.-S.; Wei, M.; Hou, Y.; Han, H.; Kelley, S. O.; Sargent, E. H. Suppressed Ion Migration in Reduced-Dimensional Perovskites Improves Operating Stability. *ACS Energy Lett.* **2019**, *4* (7), 1521–1527.

(31) Cho, J.; DuBose, J. T.; Le, A. N. T.; Kamat, P. V. Suppressed Halide Ion Migration in 2D Lead Halide Perovskites. *ACS Materials Lett.* **2020**, *2* (6), 565–570.

(32) Akriti; Shi, E.; Shiring, S. B.; Yang, J.; Atencio-Martinez, C. L.; Yuan, B.; Hu, X.; Gao, Y.; Finkenauer, B. P.; Pistone, A. J.; Yu, Y.; Liao, P.; Savoie, B. M.; Dou, L. Layer-by-Layer Anionic Diffusion in Two-Dimensional Halide Perovskite Vertical Heterostructures. *Nature Nanotechnology* **2021**.

(33) Pan, D.; Fu, Y.; Spitha, N.; Zhao, Y.; Roy, C. R.; Morrow, D. J.; Kohler, D. D.; Wright, J. C.; Jin, S. Deterministic Fabrication of Arbitrary Vertical Heterostructures of Two-Dimensional Ruddlesden–Popper Halide Perovskites. *Nature Nanotechnology* **2020**.

(34) Fu, Y.; Zheng, W.; Wang, X.; Hautzinger, M. P.; Pan, D.; Dang, L.; Wright, J. C.; Pan, A.; Jin, S. Multicolor Heterostructures of Two-Dimensional Layered Halide Perovskites That Show Interlayer Energy Transfer. *J. Am. Chem. Soc.* **2018**, *140* (46), 15675–15683.

(35) Shi, E.; Yuan, B.; Shiring, S. B.; Gao, Y.; Akriti; Guo, Y.; Su, C.; Lai, M.; Yang, P.; Kong, J.; Savoie, B. M.; Yu, Y.; Dou, L. Two-Dimensional Halide Perovskite Lateral Epitaxial Heterostructures. *Nature* **2020**, *580* (7805), 614–620.

(36) Oswald, I. W. H.; Koegel, A. A.; Neilson, J. R. General Synthesis Principles for Ruddlesden–Popper Hybrid Perovskite Halides from a Dynamic Equilibrium. *Chem. Mater.* **2018**, *30* (23), 8606–8614.

(37) Solis-Ibarra, D.; Smith, I. C.; Karunadasa, H. I. Post-Synthetic Halide Conversion and Selective Halogen Capture in Hybrid Perovskites. *Chem. Sci.* **2015**, *6* (7), 4054–4059.

(38) Elmelund, T.; Scheidt, R. A.; Seger, B.; Kamat, P. V. Bidirectional Halide Ion Exchange in Paired Lead Halide Perovskite Films with Thermal Activation. *ACS Energy Lett.* **2019**, *4* (8), 1961–1969.

(39) Zhang, Y.; Lu, D.; Gao, M.; Lai, M.; Lin, J.; Lei, T.; Lin, Z.; Quan, L. N.; Yang, P. Quantitative Imaging of Anion Exchange Kinetics in Halide Perovskites. *Proc Natl Acad Sci USA* **2019**, *116* (26), 12648.

(40) Osherov, A.; Feldman, Y.; Kaplan-Ashiri, I.; Cahen, D.; Hodes, G. Halide Diffusion in MAPbX3: Limits to Topotaxy for Halide Exchange in Perovskites. *Chem. Mater.* **2020**, *32* (10), 4223–4231.

(41) Stoumpos, C. C.; Cao, D. H.; Clark, D. J.; Young, J.; Rondinelli, J. M.; Jang, J. I.; Hupp, J. T.; Kanatzidis, M. G. Ruddlesden–Popper Hybrid Lead Iodide Perovskite 2D Homologous Semiconductors. *Chem. Mater.* **2016**, *28* (8), 2852–2867.

(42) Ma, D.; Fu, Y.; Dang, L.; Zhai, J.; Guzei, I. A.; Jin, S. Single-Crystal Microplates of Two-Dimensional Organic–Inorganic Lead Halide Layered Perovskites for Optoelectronics. *Nano Research* **2017**, *10* (6), 2117–2129.

(43) Shi, E.; Deng, S.; Yuan, B.; Gao, Y.; Akriti; Yuan, L.; Davis, C. S.; Zemlyanov, D.; Yu, Y.; Huang, L.; Dou, L. Extrinsic and Dynamic Edge States of Two-Dimensional Lead Halide Perovskites. *ACS Nano* **2019**, *13* (2), 1635–1644.

(44) Senocrate, A.; Maier, J. Solid-State Ionics of Hybrid Halide Perovskites. *J. Am. Chem. Soc.* **2019**, *141* (21), 8382–8396.

(45) Li, L.; Shang, X.; Wang, S.; Dong, N.; Ji, C.; Chen, X.; Zhao, S.; Wang, J.; Sun, Z.; Hong, M.; Luo, J. Bilayered Hybrid Perovskite Ferroelectric with Giant Two-Photon Absorption. *J. Am. Chem. Soc.* **2018**, *140* (22), 6806–6809.

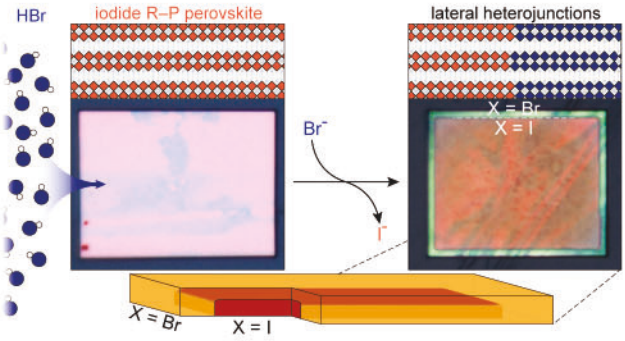
HBr
iodide R–P perovskite
lateral heterojunctions
Br⁻
I⁻
X = Br
X = I
X = Br
X = I